The Astrophysical Journal Letters, 798:L33 (6pp), 2015 January 10 doi:10.1088/2041-8205/798/2/L33

IRAS 16547−4247: A NEW CANDIDATE OF A PROTOCLUSTER UNVEILED WITH ALMA

Aya E. Higuchi[1], Kazuya Saigo[2], James O. Chibueze[2,3], Patricio Sanhueza[2], Shigehisa Takakuwa[4], and Guido Garay[5]
[1] College of Science, Ibaraki University, 2-1-1 Bunkyo, Mito 310-8512, Japan; ahiguchi@mx.ibaraki.ac.jp
[2] National Astronomical Observatory of Japan 2-21-1 Osawa, Mitaka, Tokyo 181-8588, Japan
[3] Department of Physics and Astronomy, Faculty of Physical Sciences, University of Nigeria, Carver Building, 1 University Road, Nsukka, Nigeria
[4] Academia Sinica Institute of Astronomy and Astrophysics, PO Box 23-141, Taipei 10617, Taiwan
[5] Departamento de Astronomía, Universidad de Chile, Camino El Observatorio 1515, Las Condes, Santiago, Chile
Received 2014 November 9; accepted 2014 November 27; published 2014 December 31

ABSTRACT

We present the results of continuum and ^{12}CO(3–2) and CH_3OH(7–6) line observations of IRAS 16547−4247 made with the Atacama Large Millimeter/submillimeter Array (ALMA) at an angular resolution of ∼0.″5. The ^{12}CO(3–2) emission shows two high-velocity outflows whose driving sources are located within the dust continuum peak. The alignment of these outflows does not coincide with that of the wide-angle, large-scale, bipolar outflow detected with the Atacama Pathfinder Experiment in previous studies. The CH_3OH(7–6) line emission traces an hourglass structure associated with the cavity walls created by the outflow lobes. Taking into account our results together with the position of the H_2O and class I CH_3OH maser clusters, we discuss two possible scenarios that can explain the hourglass structure observed in IRAS 16547−4247: (1) precession of a biconical jet, (2) multiple, or at least two, driving sources powering intersecting outflows. Combining the available evidence, namely, the presence of two cross-aligned bipolar outflows and two different H_2O maser groups, we suggest that IRAS 16547−4247 represents an early formation phase of a protocluster.

Key words: ISM: individual objects (IRAS 16547−4247) – ISM: jets and outflows – ISM: kinematics and dynamics – ISM: molecules – stars: formation – stars: massive

1. INTRODUCTION

Most stars, particularly high-mass stars (>8 $M_\odot$), form in clusters (Lada & Lada 2003). Stellar clusters form in dense and massive molecular clumps (size ∼ 1 pc, mass ∼ 100–1000 $M_\odot$, density ∼ 10^{4-5} cm^{-3}) (Ridge et al. 2003; Lada & Lada 2003; Lada 2010; Higuchi et al. 2009, 2010, 2013). The gas in these clumps can be significantly affected by the feedback from newly formed stars, thus blurring our understanding of cluster formation. To explore the initial conditions and details of cluster formation, it is then necessary to study molecular clouds in the early stages of evolution at high-angular resolution (e.g., Higuchi et al. 2014). High-mass stars are usually deeply embedded in their parent cloud, obscuring their early formative stages. Their formation timescales of ∼10^5 yr are short, and they form in distant clusters and associations (e.g., McKee & Ostriker 2007; Zinnecker & Yorke 2007). These factors also contribute to our poor understanding of their formation processes. High angular resolution observations are indispensable in the efforts to unveil the mystery of high-mass star formation. Millimeter and sub-millimeter interferometric observations have contributed largely to the current knowledge of high-mass star formation. The Atacama Large Millimeter/submillimeter Array (ALMA) provides the high sensitivity, angular resolution, and dynamic range to improve our understanding of the formation processes of high-mass stars.

IRAS 16547−4247 is a luminous infrared source (bolometric luminosity of 6.2 × 10^4 $L_\odot$), located at a distance of ∼2.9 kpc (Rodríguez et al. 2008). Single-dish dust continuum observations show that the IRAS source corresponds to a dense molecular clump with a mass of 1.3 × 10^3 $M_\odot$ and a radius of 0.2 pc (Garay et al. 2003). Very Large Array (VLA) radio continuum observations revealed the presence of a thermal radio jet located at the center of the core (Garay et al. 2003; Rodríguez et al. 2005). Rodríguez et al. (2005) also detected several fainter radio sources, suggesting that they are probably members of a young cluster. Garay et al. (2007) identified a large-scale bipolar ^{12}CO(J = 3–2) outflow, which is roughly oriented in the north–south direction and centered at the position of the jet source. Franco-Hernández et al. (2009) reported 1.3 mm dust continuum and SO_2 observations made with the Submillimeter Array (SMA). They found that the SO_2 emission traces a small molecular structure associated with the jet exhibiting a velocity gradient and proposed the existence of Keplerian rotation. High angular resolution observations of the high-velocity outflows toward IRAS 16547−4247 have not, however, been carried out.

In this paper, we present ∼0.″5 resolution images of the dust continuum and ^{12}CO(J = 3–2) (hereafter ^{12}CO(3–2)) and CH_3OH(v_t = 0, J_K = 7_0–6_0) (hereafter CH_3OH(7–6)) line emission using ALMA. The goal is to determine the spatial distribution and velocity structure of the gas around the center of IRAS 16547−4247 in order to explore the dynamical processes associated with the information of high-mass star formation.

2. OBSERVATIONS

IRAS 16547−4247 was observed with ALMA (Hills et al. 2010) during Early Science Cycle 0 in its extended configuration using the band 7 receivers. The observations were performed in four executions with 32 12 m antennas at an angular resolution of ∼0.″5. At the distance of IRAS 16547−4247 (d ∼ 2.9 kpc), the angular size corresponds to 0.007 pc. In this work, we present results of the 880 μm dust continuum emission, ^{12}CO(3–2) (frequency of 345.796 GHz) and CH_3OH(7–6) (frequency of 338.409 GHz) lines (see Figure 1).

The ALMA calibration includes simultaneous observations of the 183 GHz water line with water vapor radiometers that measure the water column in the antenna beam, which was later used to reduce the atmospheric phase noise. Amplitude calibration was performed using Titan. The quasars 3c279

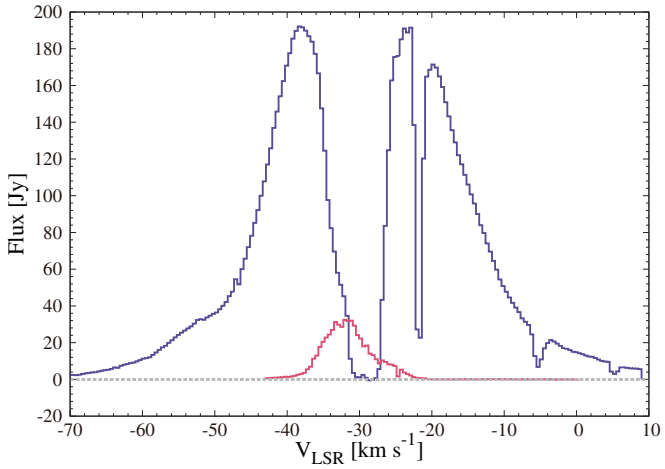

Figure 1. Average spectra of two lines detected from IRAS 16547−4247: ^{12}CO(3–2) (purple) and CH_3OH(7–6) (pink). The spectra were averaged over a region of 23″ centered on the continuum cores. This region corresponds to a box with corners at (α_{J2000}, δ_{J2000}) = [16^{h}58^{m}18^s.3, −042°52′19″.62] and (α_{J2000}, δ_{J2000}) = [16^{h}58^{m}16^s.17, −042°51′56″.72].

and J1604−446 were used to calibrate the bandpass and the complex gain fluctuations, respectively. The continuum map was obtained from a combination of all the line-free channels. Briggs weighting with a robust parameter of +0.5 was used in both continuum and line images. Data reduction was performed using version 3.4 of the Common Astronomy Software Applications package (http://casa.nrao.edu). The CASA task *CLEAN* was used to Fourier-transform the visibility data and deconvolve the dirty images at a velocity interval of 0.44 km s^{-1}.

3. RESULTS

3.1. 880 μm Continuum Emission

Figure 2(a) shows the ALMA 880 μm dust continuum map at a 0.″5 resolution. We resolved the SMA submillimeter source reported by Franco-Hernández et al. (2009) into two sources separated by ∼2″ (core A and core B in Figure 2(a)). By using the CASA task *imfit*, a Gaussian fit to the continuum emission was performed. We found that the peak flux density at 880 μm is 420 ± 30 mJy beam^{-1} for core A and 100 ± 10 mJy beam^{-1} for core B. The deconvolved sizes are 1.″1×0.″7 with a P.A. = 127° (integrated flux: 2.2 Jy) for core A and 2.″8×1.″0 with a P.A. = 69° (integrated flux: 1.7 Jy) for core B. The peak position of core A, (α_{J2000}, δ_{J2000}) = 16^{h}58^{m}17^s.217, −42°52′07″.47, agrees with the peak position derived from the SMA observations at 1.3 mm (Franco-Hernández et al. 2009).

Assuming that the emission at 880 μm corresponds to optically thin thermal dust emission, a gas-to-dust ratio of 100, a dust temperature of 100 K (Guzmán et al. 2014; Sánchez-Monge et al. 2014), a dust mass opacity of $\kappa_{880\,\mu m} = 1.8$ cm^2 g^{-1} (Ossenkopf & Henning 1994), and that this object is located at 2.9 kpc, we estimate a total H_2 mass, $M(H_2)$, of 15 $M_\odot$ for core A and 12 $M_\odot$ for core B. We stress that both cores have similar masses because core B is defined over a range with an area four times larger than that of core A.

3.2. Spectral Line Emission

Figure 1 shows the spectra of the ^{12}CO(3–2) and CH_3OH(7–6) lines integrated within a 23″×23″ region centered on the continuum source. The ^{12}CO(3–2) spectrum shows "wings" at high velocities that can be attributed to the molecular outflows. In fact, we found multiple outflows in the integrated intensity maps (see Sections 3.2.1 and 4.1, and Figures 2(b) and 4). A broad absorption line, ranging from ∼−36 to −25 km s^{-1} with a minimum at −29 km s^{-1}, and a few narrow absorption lines with the deepest one centered at −21.6 km s^{-1} are also seen in the ^{12}CO(3–2) spectrum. The narrow absorption lines are likely to be caused by foreground cold clouds, while the broad absorption line might be due to a combination of spatial filtering (e.g., resolve out) and absorption. The CH_3OH(7–6) spectrum exhibits emission in a considerably narrower velocity range than that of the ^{12}CO(3–2) spectrum.

3.2.1. Identification of Two Bipolar Molecular Outflows: The ^{12}CO(3–2) Line Emission

From Atacama Pathfinder Experiment (APEX) observations (angular resolution ∼20″), Garay et al. (2007) identified a large-scale ^{12}CO(3–2) bipolar outflow, with lobes roughly aligned in the north–south direction. The blueshifted lobe, with a velocity range from −60 to −38 km s^{-1}, extends up to ∼50″ to the south from the jet source, while the redshifted lobe, with a velocity range from −22 to −0.8 km s^{-1}, extends up to ∼50″ to the north. The spectrum of the spatially integrated ^{12}CO(3–2) line emission observed with ALMA is quite similar to the APEX ^{12}CO(3–2) spectrum centered on the jet source, and both show broad absorption lines. The broad absorption line feature is most likely produced by the colder, collapsing envelope surrounding the central sources.

Figure 2(b) shows ^{12}CO(3–2) integrated intensity maps of the blueshifted (velocity range from −70 to −45.8 km s^{-1}) and redshifted (velocity range from −15.9 to +8.8 km s^{-1}) wing emission. The dust continuum emission is overlaid with black contours. From Figure 2(b), we identified two bipolar outflows, one aligned in the northeast–southwest direction (Outflow-1, R1-B1 in Figure 2(b)), and the other aligned in the northwest–southeast direction (Outflow 2, R2-B2 in Figure 2(b)). The velocity ranges were selected to separate distinct features of both outflows lobes. These outflows appear at considerably smaller angular scales than the wide-angle bipolar outflow detected with APEX and their position angles are different.

We found another redshifted component associated with the S1 H_2O maser cluster to the south of the continuum peak. For S1, Rodríguez et al. (2008) suggested the existence of a YSO candidate associated with this component from their VLA observations. This YSO may have a different systemic velocity from that of the central continuum source; thus, the ^{12}CO(3–2) component appeared to be dominantly redshifted with reference to the systemic velocity of the central object. In fact, we found a faint blueshifted component, with a velocity range from −55 to −32 km s^{-1}, associated with S1. Our observations also support the existence of another source as suggested by Rodríguez et al. (2008). For discussion, we also plot the positions of the H_2O (g1 and g2 in Figure 2(a)) and CH_3OH maser clusters (pink crosses in Figure 4) detected by Franco-Hernández et al. (2009) and Voronkov et al. (2006), respectively.

3.2.2. Shock-Enhanced Regions: The CH_3OH(7–6) Line Emission

There are several transitions of CH_3OH between 338.3 GHz and 338.7 GHz and many of them were detected with ALMA. For discussion here, we selected the strongest line corresponding to $v_t = 0$, $J_K = 7_0$–6_0, A-type transition at 338.409 GHz (Kristensen et al. 2010), hereafter CH_3OH(7–6).

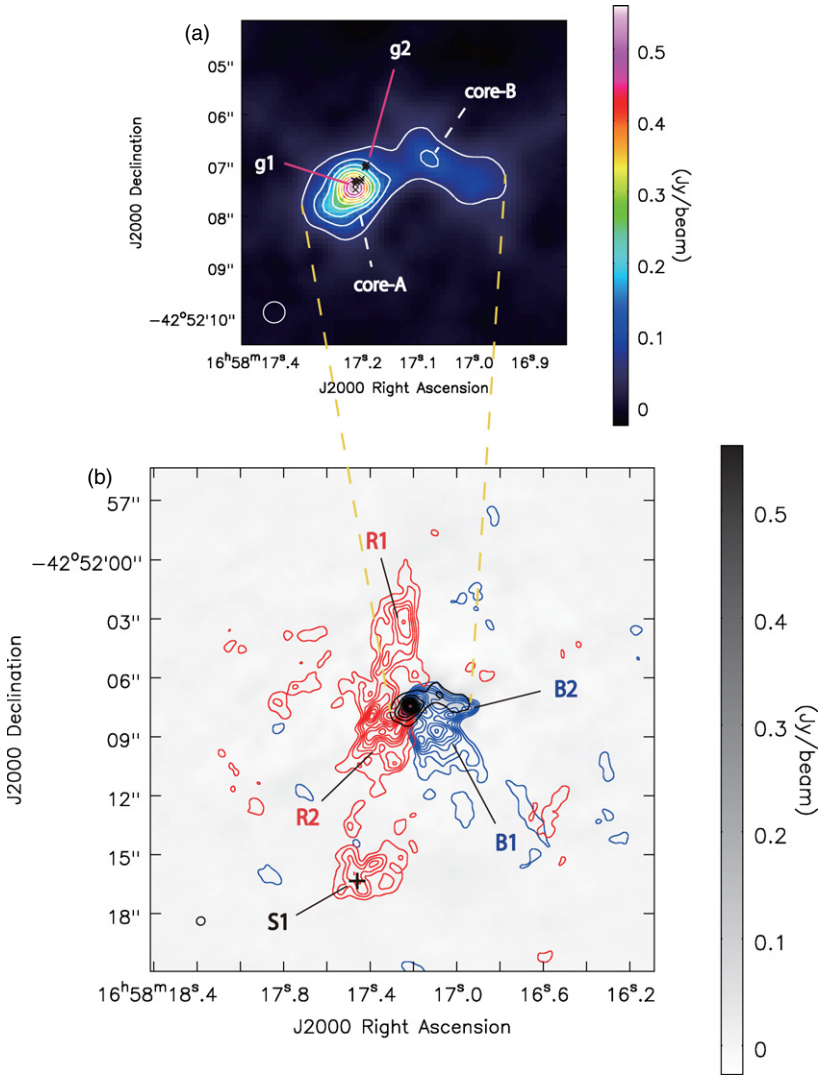

Figure 2. (a) ALMA 880 μm continuum emission (color and contours) from IRAS 16547−4247. The small crosses (black) mark the positions of the water maser clusters named g1 and g2 in Franco-Hernández et al. (2009). The white contours range from 10% to 90% of the peak emission in steps of 10%. (b) Integrated intensity map of the ^{12}CO(3–2) outflows and the continuum emission (black contours). The blue represents blueshifted gas, while the red represents the redshifted gas. The integrated velocity range of ^{12}CO(3–2) for the blueshifted side is from −70.0 to −45.8 km s^{-1}, while for the redshifted side is from −15.9 to +8.8 km s^{-1}. The contours for integrated intensity maps, with intervals of 3σ, start from the 3σ level (1σ = 0.6 Jy beam^{-1} km s^{-1} for both blueshifted and redshifted gas). The black cross marks the position of the water masers called S1 in Franco-Hernández et al. (2009). The grayscale bar shows the flux density of dust continuum emission.

Figure 3(a) shows the velocity-integrated intensity map of the CH_3OH(7–6) emission (color and contours). The CH_3OH(7–6) emission from the central region is strong and well correlated with the dust continuum emission. At fainter levels, the CH_3OH(7–6) emission appears as weak filaments elongated to the northeast, southeast, northwest, and southwest, forming an hourglass structure. In order to investigate the detailed velocity structure of the CH_3OH(7–6) emission, we produced first and second moment maps (Figures 3(b) and (c), respectively). In the first moment map, we see toward the central region a similar velocity gradient as is seen in SO_2, which might be Keplerian rotation (Franco-Hernández et al. 2009). In the second moment map, the region associated with dust continuum emission exhibits a large velocity dispersion of ∼10 km s^{-1}.

CH_3OH is predominantly formed on grain surfaces (Watanabe & Kouchi 2002; Fuchs et al. 2009). Although small CH_3OH abundances can be found in cold, quiescent environments (Garrod et al. 2007; Sanhueza et al. 2013), CH_3OH is largely released into the gas phase by processes related to active star formation: heating from protostars or sputtering of the grain mantles produced by the interaction of molecular outflows and the ambient gas (e.g., Sakai et al. 2013; Yanagida et al. 2014). To compare the CH_3OH(7–6) emission with that of the outflows, we show the second moment map of the CH_3OH(7–6) emission overlaid with the velocity integrated maps of the blueshifted and redshifted ^{12}CO(3–2) emission in Figure 4.

We find that the northeast and southwest walls of the CH_3OH(7–6) hourglass structure are located at the edge of the northeast and southwest lobes of Outflow 1, respectively, suggesting a relationship. We also find that the redshifted component of Outflow 2, R1, is associated with the ring-like wall located southeast of the central source. In addition, there is a good correlation between the spatial distribution of the CH_3OH(7–6) emission and the CH_3OH maser spots. From all these results, we conclude that the CH_3OH(7–6) emission traces zones of post-shocked gas produced by the interaction of multiple outflows with the ambient gas within the IRAS 16547−4247 region.

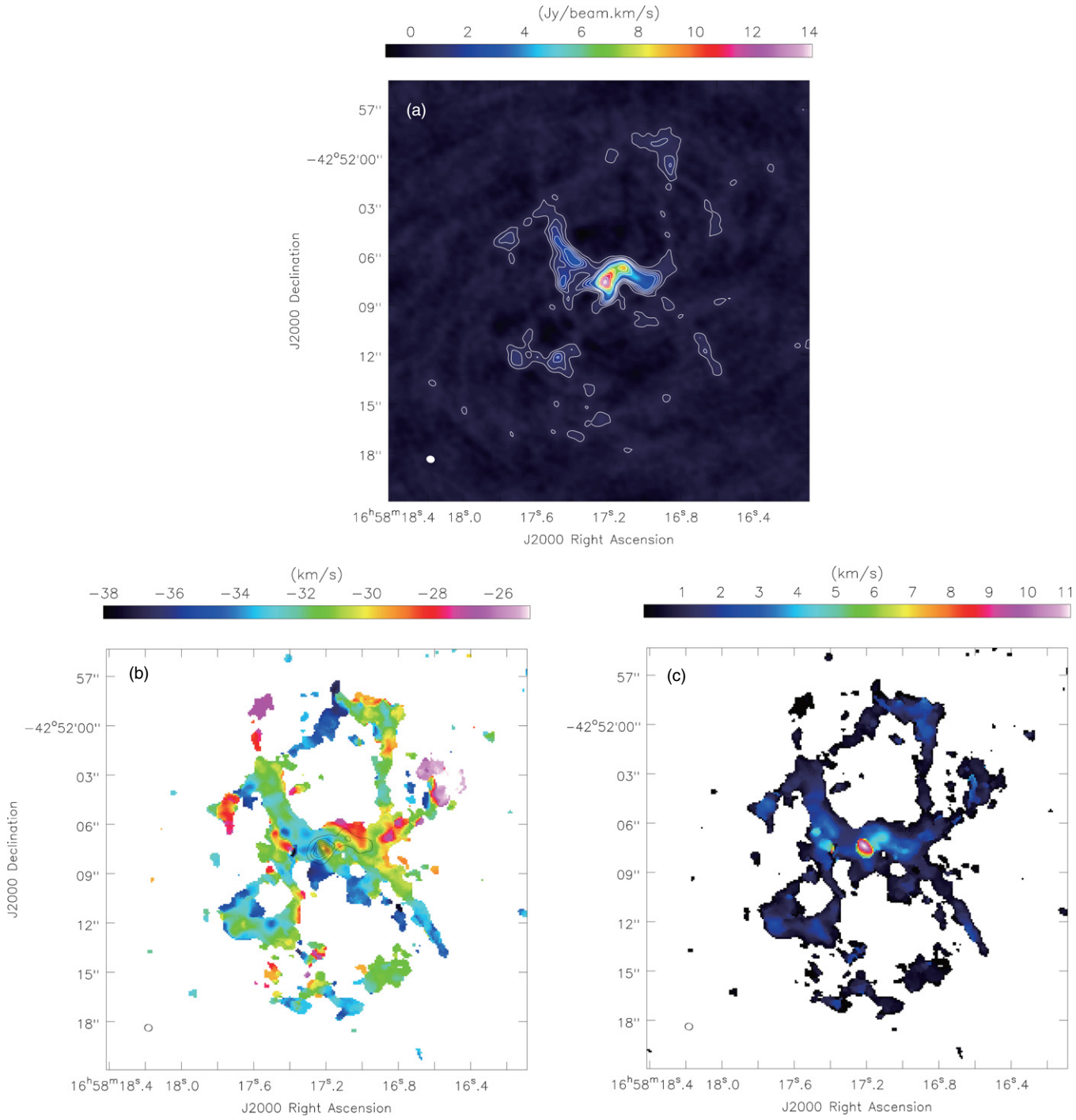

Figure 3. (a) Integrated intensity map of the CH_3OH(7–6) emission (color and contours). Contours start first from 3σ to 30σ increasing in intervals of 3σ levels and then they continue in step of 10σ up to the 100σ level ($1\sigma = 0.15$ Jy beam^{-1} km s^{-1}). (b) Dust continuum emission (black contours) superposed on the first moment map of CH_3OH(7–6) emission (color). (c) The second moment map of CH_3OH(7–6) emission (color).

4. DISCUSSION

4.1. Maser Distribution and ^{12}CO(3–2) Outflows

H_2O masers (Franco-Hernández et al. 2009) and class I CH_3OH maser clusters (Voronkov et al. 2006) have been detected toward the IRAS 16547−4247 region (see Figures 2(a) and 4). In high-mass star forming regions, H_2O masers are predominantly located within a few milliarcseconds from the central driving sources, tracing gas motions in the vicinity of the protostar (Torrelles et al. 2011; Chibueze et al. 2014). On the other hand, class I CH_3OH maser clusters are usually excited at the shocked interface between a high-velocity jet, or outflow, and the ambient gas cloud. The g1 and g2 H_2O masers detected by Franco-Hernández et al. (2009) are located within the continuum peak and close to the centers of the two bipolar outflows (see Figures 2(a) and (b)), suggesting that they could mark the position of the driving sources of the outflows. Higher angular resolution observations are required to identify the driving sources and make a more precise relation with g1 and g2. In addition, the H_2O masers located at the position of

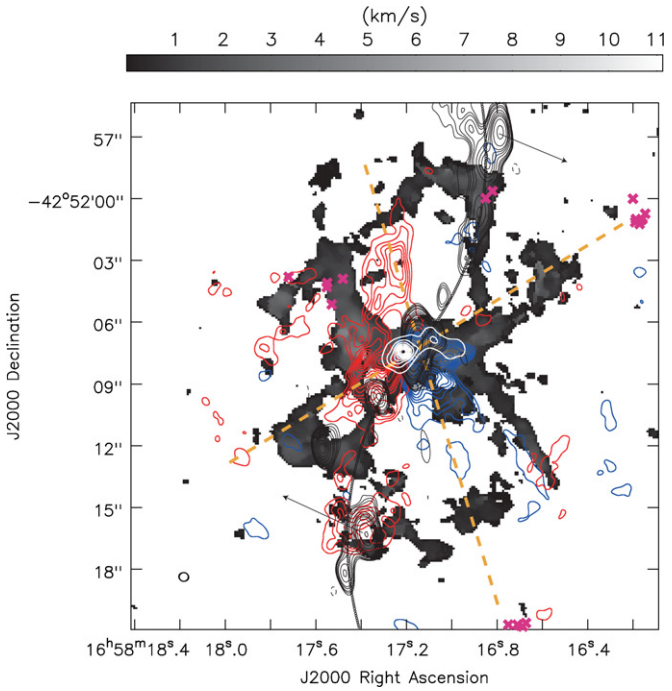

Figure 4. Second moment map of the CH_3OH(7–6) emission (grayscale) and integrated intensity map of the ^{12}CO(3–2) outflows (contours). The integrated velocity range for the blueshifted and redshifted side are the same in Figure 2(b). The contours with the intervals of the 3σ levels start from the 3σ levels (see Figure 2(b)). White contours show the dust continuum emission as in Figure 2(a). Black contours show the VLA continuum emission detected by Rodríguez et al. (2008). The pink crosses mark the positions of the class I CH_3OH masers listed in Voronkov et al. (2006). The dashed lines indicate the direction of outflows estimated by using the position of maser clusters.

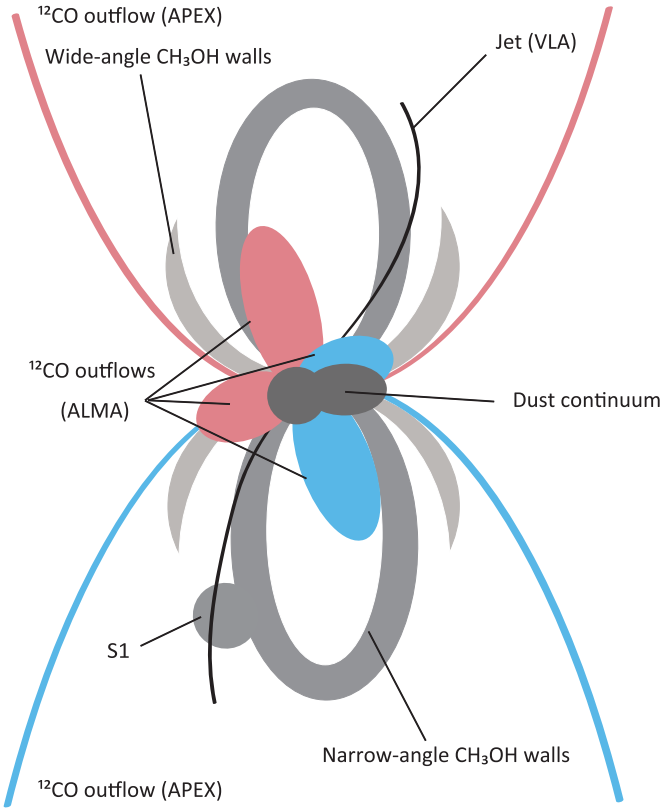

Figure 5. Schematic illustration of the complex environment revealed by ALMA in IRAS 16547−4247. The dust continuum cores are surrounded by interacting outflows, cavity walls, and an ionized jet.

S1 are most likely excited by a different YSO, thus adding to the multiplicity of the protostars in the region.

Figure 4 indicates the spatial distribution of the four class I CH_3OH maser clusters (Voronkov et al. 2006) present within the field of the ALMA observations. The clusters located northeast and southwest of the central source roughly aligns with Outflow 1, while the maser cluster seen toward the northwest aligns with the blueshifted lobe of Outflow 2, B2. The dashed lines in Figure 4 indicate the directions of the outflows estimated by using the position of the CH_3OH maser clusters. The northern cluster coincides with the location of the jet knots of Rodríguez et al. (2008), and may have been excited by the shock influence of the jet. A schematic diagram to visualize the star formation activities in the region based on previous observations and our ALMA results is shown in Figure 5.

4.2. The Nature of the IRAS 16547−4247 Region

In an attempt to explain the observed morphology of the shocks traced by the CH_3OH(7–6) emission, we discuss two possible scenarios that may be responsible for the hourglass structure seen in Figures 3 and 4.

The first of the plausible scenarios is the precession of the biconical jet reported by Rodríguez et al. (2008) (see Figure 4). The interaction of the high-velocity precessing jet with the dense ambient medium results in strong shocks, which will trace a larger biconical structure (as seen in the morphology of the narrow-angle CH_3OH(7–6) wall). Assuming that the opening angle of the observed narrow-angle CH_3OH(7–6) wall is the angle subtended by the minor axis at a distance of one-half the major axis, we derived the opening angle of the narrow-angle CH_3OH(7–6) wall to be ∼45°. The jet has an opening angle of 15°, implying that the jet will need to precess through 30° to create the observed narrow-angle CH_3OH(7–6) wall. Rodríguez et al. (2008) assumed that the jet seems to be precessing linearly with time and derived a precession rate, β, of 0.°08 yr^{-1} ($\beta = \alpha v$, with $\alpha \sim 2.°3$ $arcsec^{-1}$ and a jet velocity, v, of ∼490 km s^{-1} as in Rodríguez et al. 2008). Assuming that these rates of the N1 and S1 represent the precession rate of the entire jet, we estimated that it would take the collimated precessing jet about ∼380 yr to produce the observed morphology.

The second scenario is that of multiple, or at least two, driving sources powering intersecting outflows. Garay et al. (2003) showed two outflow lobes, which may be suggestive of a single driving source. However, ^{12}CO(3–2) at high-angular resolution with ALMA shows two outflows; one aligned in the northwest–southeast direction, and the other one aligned in the northeast–southwest direction (Figures 2(b) and 4). This points to the multiplicity of the protostars driving outflows in the region. This agrees with the distribution of the class I CH_3OH masers of Voronkov et al. (2006), which also suggest the presence of more than one outflow source in the region. The complexity of the outflow structures could be explained by the interaction of the outflowing materials from different driving sources.

We thank the anonymous referee for constructive comments which helped to improve this manuscript. We also thank the ALMA staff for the observations during the commissioning stage. G.G. acknowledges support from CONICYT project PFB-06. This Letter makes use of the following ALMA data: ADS/JAO.ALMA#2011.0.00419.S. ALMA is a partnership of

the ESO (representing its member states), NSF (USA), and NINS (Japan), together with NRC (Canada), NSC, and ASIAA (Taiwan), in cooperation with the Republic of Chile. The Joint ALMA Observatory is operated by the ESO, AUI/NRAO, and NAOJ. Data analysis were carried out on a common use data analysis computer system at the Astronomy Data Center, ADC, of the National Astronomical Observatory of Japan. Finally, we acknowledge Masao Saito for his contribution to our study.

REFERENCES

Chibueze, J. O., Omodaka, T., Handa, T., et al. 2014, ApJ, 784, 114
Franco-Hernández, R., Moran, J. M., Rodríguez, L. F., & Garay, G. 2009, ApJ, 701, 974
Fuchs, G. W., Cuppen, H. M., Ioppolo, S., et al. 2009, A&A, 505, 629
Garay, G., Brooks, K. J., Mardones, D., & Norris, R. P. 2003, ApJ, 587, 739
Garay, G., Mardones, D., Bronfman, L., et al. 2007, A&A, 463, 217
Garrod, R. T., Wakelam, V., & Herbst, E. 2007, A&A, 467, 1103
Guzmán, A. E., Garay, G., Rodríguez, L. F., et al. 2014, ApJ, 796, 117
Higuchi, A. E., Chibueze, J. O., Habe, A., Takahira, K., & Takano, S. 2014, AJ, 147, 141
Higuchi, A. E., Kurono, Y., Naoi, T., et al. 2013, ApJ, 765, 101
Higuchi, A. E., Kurono, Y., Saito, M., & Kawabe, R. 2010, ApJ, 719, 1813
Higuchi, A. E., Kurono, Y., Saito, M., & Kawabe, R. 2009, ApJ, 705, 468
Hills, R. E., Kurz, R. J., & Peck, A. B. 2010, Proc. SPIE, 7733
Kristensen, L. E., van Dishoeck, E. F., van Kempen, T. A., et al. 2010, A&A, 516, AA57
Lada, C. J. 2010, RSPTA, 368, 713
Lada, C. J., & Lada, E. A. 2003, ARA&A, 41, 57
McKee, C. F., & Ostriker, E. C. 2007, ARA&A, 45, 565
Ossenkopf, V., & Henning, T. 1994, A&A, 291, 943
Ridge, N. A., Wilson, T. L., Megeath, S. T., Allen, L. E., & Myers, P. C. 2003, AJ, 126, 286
Rodríguez, L. F., Garay, G., Brooks, K. J., & Mardones, D. 2005, ApJ, 626, 953
Rodríguez, L. F., Moran, J. M., Franco-Hernández, R., et al. 2008, AJ, 135, 2370
Sakai, T., Sakai, N., Foster, J. B., et al. 2013, ApJL, 775, L31
Sánchez-Monge, Á., Beltrán, M. T., Cesaroni, R., et al. 2014, A&A, 569, A11
Sanhueza, P., Jackson, J. M., Foster, J. B., et al. 2013, ApJ, 773, 123
Torrelles, J. M., Patel, N. A., Curiel, S., et al. 2011, MNRAS, 410, 627
Yanagida, T., Sakai, T., Hirota, T., et al. 2014, ApJL, 794, L10
Voronkov, M. A., Brooks, K. J., Sobolev, A. M., et al. 2006, MNRAS, 373, 411
Watanabe, N., & Kouchi, A. 2002, ApJL, 571, L173
Zinnecker, H., & Yorke, H. W. 2007, ARA&A, 45, 481